EPJ manuscript No.
(will be inserted by the editor)

Particle Transport in Graphene Nanoribbon Driven by Ultrashort Pulses

D. Babajanov[1], D.U. Matrasulov[1] and R. Egger[2]

[1] Turin Polytechnic University in Tashkent, 17. Niyazov Str., 100095, Tashkent, Uzbekistan
[2] Institut für Theoretische Physik, Heinrich-Heine-Universität, D-40225 Düsseldorf, Germany

the date of receipt and acceptance should be inserted later

Abstract. We study charge transport in a graphene zigzag nanoribbon driven by an external time-periodic kicking potential. Using the exact solution of the time-dependent Dirac equation with a delta-kick potential acting in each period, we study the time evolution of the quasienergy levels and the time-dependent optical conductivity. By variation of the kicking parameters, the conductivity becomes widely tunable.

PACS. 72.80.Vp – 78.67.Wj – 73.22.Pr

arXiv:1409.2719v2 [cond-mat.mes-hall] 3 Oct 2014

1 Introduction

Ever since its experimental discovery a decade ago, the physics of graphene has been a hot topic in condensed matter physics, see Refs. [1,2,3,4,5,6,7] for reviews. One of the most intensely studied class of problems concerns electronic transport in bulk or confined graphene monolayers. We here focus on the particle dynamics in externally driven graphene samples, where a general goal is to achieve tunability of charge transport. A rich variety of predicted and observed phenomena due to time-dependent fields have been reported in recent publications [8,9,10,11, 12,13,14,15].

In particular, Ref. [8] argues that time-periodic spin-orbit interactions lead to an interesting time evolution of the spin polarization and of the optical conductivity. Particle transport can also be induced by a time-dependent elastic deformation field [9], or in a.c. driven graphene nanoribbons, where by adopting a tight-binding model, the authors of Ref. [13] found a strong dependence of transport properties on the geometry of the ribbon edges. Furthermore, Ishikawa [14] studied electron transport in graphene perturbed by a time-periodic vector potential, which results in an enhancement of interband transitions. Finally, electron transport and current resonances in the presence of a time-dependent scalar potential barrier have been studied in Ref. [15], where a resonant enhancement of both electron backscattering and the currents across and along the barrier was reported when the modulation frequencies satisfy certain resonance conditions.

Ultrafast dynamics and particle transport in graphene driven by ultrashort optical pulses have also been studied recently [16,17,18,19,20,21,22]. The experimental observation of a bright broadband photoluminescence in graphene interacting with femtosecond laser pulses was reported in Ref. [18]. Moreover, the authors of Ref. [22] have studied the modification of the bandstructure under ultrashort optical pulses and the carrier dynamics caused by the optical response of graphene, arguing that the electron dynamics in the time-dependent electric field of the laser pulse becomes irreversible, with a large residual conduction band population. In addition, the formation of a laser-induced band gap was discussed in Ref. [20].

In this paper, we study electron transport in graphene nanoribbons interacting with an external time-periodic scalar potential represented by a sequence of δ-kicks. The setup is schematically shown in Fig. 1. Such a potential could be created by applying laser pulses to free-standing samples. Using the exact solution of the time-dependent Dirac equation within one kicking period, we compute the transport properties of the system, such as the probability current and the optical conductivity, as a function of time. As we have discussed above, periodically driven graphene could be realized through the interaction with a.c. voltages [13], pulsed laser fields [23], surface acoustic waves [24], or time-periodic straining [9]. Here we focus on the case of ultrashort optical pulses [16,17,18,19].

Let us mention at this stage that some time ago, both the classical and the quantum dynamics of systems interacting with a delta-kicking potential have been extensively studied in the context of nonlinear dynamics and quantum chaos theory [25,26,27]. A remarkable feature of periodically driven quantum systems is the quantum localization phenomenon, which implies a suppression of the growth of the average kinetic energy with time; for the corresponding classical system, this energy grows linearly in time. However, the case of delta-kicked graphene nanoribbons is more complicated due to the kicking-field-induced modification of the graphene bandstructure.

Send offprint requests to: d.matrasulov@polito.uz

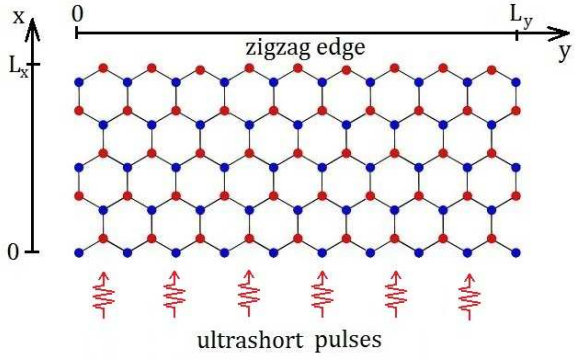

Fig. 1. Sketch of a kicked zig-zag graphene nanoribbon of width L_x and length L_y. Ultrashort periodic pulses applied to the nanoribbon act as kicking potential.

Such a modification of the bandstructure is the underlying reason for the interesting electronic and transport phenomena found in driven graphene. The main effect of the driving force is to cause inter- and intra-band transitions, leading to excitation and "ionization" of valence-band electrons to the conduction band. Another effect caused by driving fields in graphene is a band-gap opening or widening [20], which allows one to tune the electronic properties using an external time-dependent field. Below, we analyze the time evolution of the quasi-bandstructure and of the optical conductivity in delta-kicked graphene nanoribbons. We find that the quasienergy levels exhibit intra-band crossings and inter-band anticrossings, where the time-dependent effective density of states reaches a local maximum when the anticrossings take place. This may increase the number of charge carriers in the conduction band, with a subsequent increase of the current and of the optical conductivity. Indeed, as is shown by our analysis of the time-dependent conductivity in Sec. 3, depending on the kicking parameters, the conductivity may monotonically grow in time, while in other kicking regimes, such a growth is suppressed.

The remainder of this paper is organized as follows. In Sec. 2 we briefly recall the Dirac equation for graphene zigzag nanoribbons, basically following the approach of Brey and Fertig [28], and discuss the solution of the time-dependent Dirac equation in the presence of the δ-kicking potential. This solution is then utilized to compute the time evolution of the quasi-bandstructure, and, in Sec. 3, the optical conductivity in different kicking regimes. Finally, Sec. 4 contains some concluding remarks. Below we often use units where $\hbar = 1$.

2 Kicked graphene nanoribbon

2.1 Unperturbed Hamiltonian

In this work we study the electronic behavior of kicked zigzag graphene nanoribbons, see Fig. 1 for an illustration, within the Dirac equation approach [28]. It is well established that low-energy quasiparticles in an extended graphene sheet are accurately described by the massless two-dimensional (2D) Dirac Hamiltonian [1]

$$H_0 = v_F \begin{pmatrix} 0 & p_x - ip_y \\ p_x + ip_y & 0 \end{pmatrix}, \tag{1}$$

where $p_x = -i\partial_x$, $p_y = -i\partial_y$, and $v_F \approx 10^6$ m/sec denotes the Fermi velocity. The 2×2 matrix structure of H_0 is with respect to sublattice space, corresponding to the (A/B-type) basis atoms of graphene's honeycomb lattice [1]. Since we do not take into account electron-electron interaction effects here, the two different valleys (K points) as well as the two spin projections decouple, and we can focus on a single-valley spinless system in Eq. (1). The spinor eigenstates of the zigzag nanoribbon with periodic boundary conditions along the longitudinal y-direction, see Fig. 1, are written as

$$\psi(x,y) = \frac{e^{ik_y y}}{\sqrt{L_y}} \Phi(x), \quad \Phi(x) = \begin{pmatrix} \phi_A(x) \\ \\ \phi_B(x) \end{pmatrix}, \tag{2}$$

where k_y is the conserved wave number along the y-direction. Periodic boundary conditions yield $k_y = 2\pi n_y/L_y$ with integer n_y. To take into account the zigzag edges at $x = 0$ and $x = L_x$, where L_x is the width of the nanoribbon, we impose the boundary conditions [28]

$$\phi_A(L_x) = \phi_B(0) = 0, \tag{3}$$

and put $0 \le x \le L_x$ henceforth.

Next we summarize the spinor solutions $\psi_n(x,y)$ solving the stationary Dirac equation for eigenenergy E_n in the absence of the kicking potential,

$$H_0\psi_n(x,y) = E_n\psi_n(x,y), \quad n = (n_x, n_y), \tag{4}$$

where the integer n_x serves as a band index and n_y parametrizes k_y. The boundary conditions (3) imply that the eigenvalues of Eq. (4) are obtained from the transcendental equation [28]

$$\frac{k_y - z}{k_y + z} = e^{-2L_x z}, \tag{5}$$

which admits two type of solutions, namely (i) confined modes (standing waves), and (ii) surface states.

We start by discussing solutions of type (i), which are purely imaginary, $z_{n_x} = ik_x$, and lead to the eigenenergies

$$E_n = \pm v_F \sqrt{k_x^2 + k_y^2}, \tag{6}$$

where the upper (lower) sign corresponds to the conduction (valence) band. Equation (5) now simplifies to

$$k_y = \frac{k_x}{\tan(k_x L_x)}, \tag{7}$$

and solutions for k_x (labeled by $n_x = 1, 2, \ldots$) correspond to confined modes. The respective eigenstate (2), with the energy E_n in Eq. (6), has the transverse wavefunction

$$\Phi_n(x) = \mathcal{N}_n \begin{pmatrix} \sin(k_x x) \\ \pm\frac{i}{E_n}[-k_x \cos(k_x x) + k_y \sin(k_x x)] \end{pmatrix}, \tag{8}$$

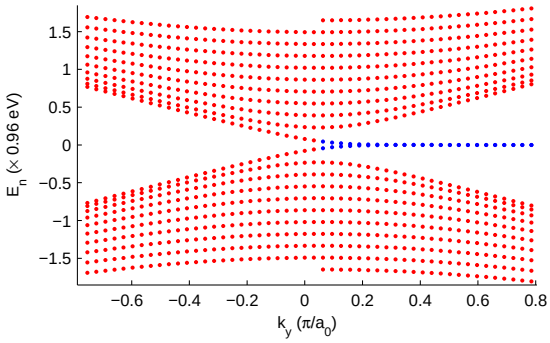

Fig. 2. Band structure of unperturbed graphene nanoribbon. The red dots indicate eigenenergies of confined modes, and the blue dots correspond to surface states. The nanoribbon has width $L_x = 4.92$ nm and length $L_y = 12.3$ nm, and $a_0 = 0.246$ nm is the lattice unit.

with normalization constant $\mathcal{N}_n$.

Next we turn to surface state [type (ii)] solutions. These correspond to purely real $z = k_x$ in Eq. (5), where the eigenstate reads

$$\Phi_n(x) = \mathcal{N}'_n \begin{pmatrix} 2\sinh(k_x x) \\ \frac{1}{E_n}\left[k_y \sinh(k_x x) - k_x \cosh(k_x x)\right] \end{pmatrix}. \quad (9)$$

The eigenenergy is now given by

$$E_n = \pm\sqrt{k_y^2 - k_x^2}, \quad (10)$$

and $\mathcal{N}'_n$ is another normalization constant. The surface state energies equal zero for sufficiently large positive k_y, but they are absent for $k_y < 0$. In Fig. 2, the resulting bandstructure of a typical graphene zigzag nanoribbon is plotted.

2.2 Including the kicking potential

We are now ready to include the external driving potential. We consider a periodic sequence of delta-kicks of kicking strength ε and period T. (No confusion with the symbol for temperature should arise here; we always consider the zero-temperature limit.) Writing $H = H_0 + V\,\mathrm{diag}(1,1)$, the additional term is given by the time-periodic scalar potential,

$$V(x,t) = \varepsilon\cos(2\pi x/\lambda)\sum_{l=0}^{\infty}\delta(t - lT), \quad (11)$$

where λ is the wavelength of the kicking pulse. Experimentally, such delta-kicks could be realized by standing-wave laser pulses [29,30,31], or by half-cycle laser pulses [32]. For instance, the delta-kicked quantum rotor, representing a well-known paradigm of quantum chaos theory, can be experimentally realized in ultracold atoms that interact with the periodic standing wave of a near-resonant laser field [29]. Significant progress concerning the experimental realization of graphene interacting with ultrashort laser pulses has also been reported recently [17,18,19]. Combining the experimental methods in Refs. [29,30,31,32] with those in Refs. [17,18,19] could allow to implement the delta-kicked graphene nanoribbon discussed here in the lab.

The dynamics of a state $\Psi = \Psi(x,y,t)$ is then governed by the time-dependent 2D Dirac equation, $i\partial_t\Psi = H\Psi$. To solve this equation, we expand $\Psi(x,y,t)$ in terms of the complete set of eigenfunctions of the unperturbed graphene zigzag nanoribbon discussed in Sec. 2.1,

$$\Psi(x,y,t) = \sum_n A_n(t)\psi_n(x,y), \quad (12)$$

where $n = (n_x, n_y)$ and the summation implicitly includes the $\pm$ sign for the conduction and valence band, respectively. To ensure normalization, the initial values (at time $t = 0$) of the complex-valued expansion coefficients $A_n(t)$ in Eq. (12) satisfy the condition

$$\sum_n |A_n(0)|^2 = 1. \quad (13)$$

Within one time period, the amplitude A_n then follows the time evolution

$$A_n(t+T) = \sum_{n'} V_{nn'} e^{-iE_{n'}T} A_{n'}(t) \quad (14)$$

where E_n is the unperturbed eigenenergy of the respective mode, see Sec. 2.1, and we define the matrix elements

$$V_{nn'} = \int_0^{L_x} dx \int_0^{L_y} dy\ \psi^\dagger_{n'}(x,y) e^{i\varepsilon\cos(2\pi x/\lambda)}\psi_n(x,y), \quad (15)$$

where nonzero matrix elements exist only for $n_y = n'_y$ due to the translation invariance in y-direction. In calculating these matrix elements, we use a well-known Bessel function expansion formula for the exponential term.

In numerical calculations, one may choose only a few non-zero initial coefficients $A_n(0)$ subject to Eq. (13). In particular, we tested the impact of using different choices for $A_n(0)$, such as randomly chosen or equally distributed values. All choices were found to give qualitatively similar results for the time-evolved state $\Psi(t)$ after many kicks. For the calculations presented below, we chose a random distribution for the coefficients $A_n(0)$ containing ≈ 15 non-zero entries, where we take into account only states with energy E_n below the Fermi level. The Fermi level is here assumed at the neutrality point, i.e., $E_F = 0$, in order to maximally emphasize the Dirac fermion nature of the graphene nanoribbon. Our procedure for choosing the initial values for the A_n coefficients mimics the zero-temperature average over the filled Fermi sea. We have carefully checked that different initial values lead to the same physical results after a short initial transient.

Given the wave function, one can compute different characteristics of the carrier dynamics and, in particular, investigate charge transport in a kicked graphene nanoribbon. In Fig. 3, the time evolution of quasienergy levels

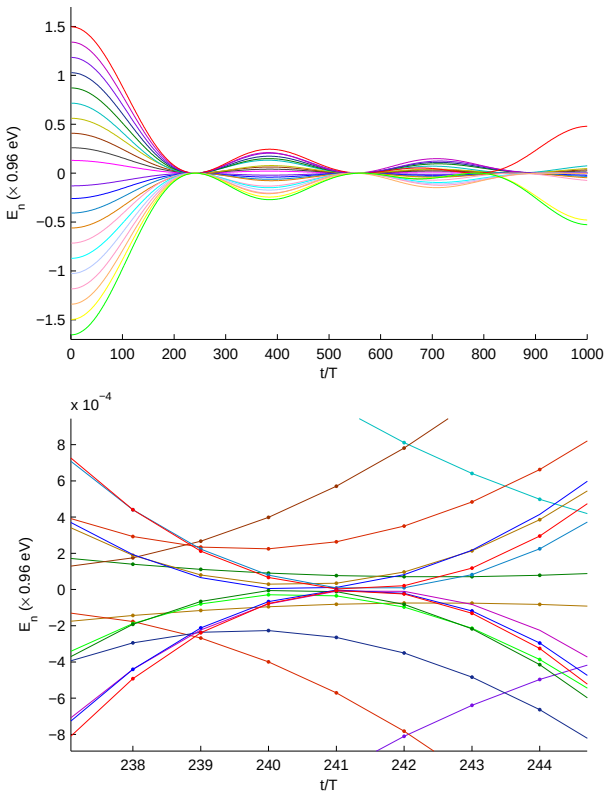

Fig. 3. The upper panel shows the time evolution of a few selected quasienergy levels. The lower panel shows the same but on a magnified scale near the first level (anti-)crossing. The ribbon width L_x and length L_y were chosen as in Fig. 2. The kicking strength is $\varepsilon = 2.7 \times 10^{-13}$ eVs, with period $T = 0.1$ fs and wavelength $\lambda = 2.46$ nm.

is shown for a few selected states. We observe several crossings of the levels within the conduction (or within the valence) band. However, levels coming from different bands exhibit anticrossing, where levels closely approach each other up to some time when they start to separate again. After a certain number of kicks, one can then again observe crossings or anticrossings, where intra- and interband transitions become more frequent. Since initially the valence band is filled, this can lead to an increase in the number of electrons in the conduction band, and thereby to current flow. A related enhancement of intra- and inter-band transitions has also been reported in Ref. [22] for graphene subject to ultrashort laser pulses. When the quasienergy levels separate from each other again after the crossing or anticrossing, intra- and interband transitions become less frequent, and one can expect a decrease in the current. Such features indeed appear in the conductivity, as we study next.

3 Optical conductivity

The interaction of external electromagnetic fields with solids generally causes a modification of their electronic properties and, in particular, of the bandstructure [22,33]. Using the solution of the time-dependent Dirac equation for delta-kicking potential discussed in Sec. 2, one can compute such modifications in the bandstructure, see Fig. 3. In this section, we focus on the optical conductivity of our system, which represents an important observable of experimental interest and can provide precious insights about the transport mechanisms at play in kicked graphene nanoribbons.

Within linear response theory, the Kubo formula yields for the diagonal elements of the time-dependent conductivity tensor ($\alpha = x, y$) [34]

$$\sigma_{\alpha\alpha}(x,y;t,\omega) = \frac{e^2}{\omega}\int_0^\infty d\tau e^{-i\omega\tau} \times \langle [J_\alpha(x,y,t), J_\alpha(x,y,t-\tau)]\rangle \,, \tag{16}$$

where $[,]$ denotes the commutator and the particle current density along the α-direction is [1]

$$J_\alpha(x,y,t) = v_F \Psi^\dagger(x,y,t)\sigma_\alpha \Psi(x,y,t), \tag{17}$$

with standard Pauli matrices $\sigma_{\alpha=x,y}$ acting in sublattice space. The average in Eq. (16) is taken with respect to the filled Fermi sea at the initial time $t = 0$, present before the kicking potential is switched on. In Eq. (16), we focus on the long-wavelength limit by probing the two current operators appearing in the Kubo formula at the same point in space. In terms of the expansion coefficients $A_n(t)$ appearing in the expansion (12), Eq. (17) takes the form

$$J_\alpha(x,y,t) = v_F \sum_{nn'} A^*_{n'}(t) A_n(t) \psi^\dagger_{n'}(x,y)\sigma_\alpha \psi_n(x,y), \tag{18}$$

where A^* denotes the complex conjugate of A. Inserting Eq. (18) into Eq. (16), the conductivity at time t follows as a lengthy (but straightforwardly obtained) expression involving the time-dependent coefficients $\{A_n(t')\}$ for $0 < t' < t$. As described in Sec. 2.2, the zero-temperature average over the filled Fermi sea is implemented by choosing suitable initial values for those coefficients. Below we discuss the time-dependence of the conductivity averaged over the sample area and taken in the $\omega \to 0$ limit,

$$\sigma_{\alpha\alpha}(t) = \lim_{\omega\to 0} \mathrm{Re} \int_0^{L_y} \frac{dy}{L_y} \int_0^{L_x} \frac{dx}{L_x} \sigma_{\alpha\alpha}(x,y;t,\omega). \tag{19}$$

Figure 4 shows numerical results for $\sigma_{xx}(t)$ for representative kicking potential parameters. We observe that $\sigma_{xx}(t)$ grows during some initial time interval, followed by a suppression of the growth along with the development of oscillatory behavior. These features can be linked to the presence of crossings and anticrossings in the bandstructure, as discussed above.

Next, Fig. 5 presents $\sigma_{xx}(t)$ for a fixed kicking period, $T = 1$ fs, but now for different values of the kicking strength ε. For the shown regime of rather short times, the conductivity monotonically grows in time. Clearly, for larger kicking strength, $\sigma_{xx}(t)$ grows more rapidly, where the slope of the growth is approximately proportional to

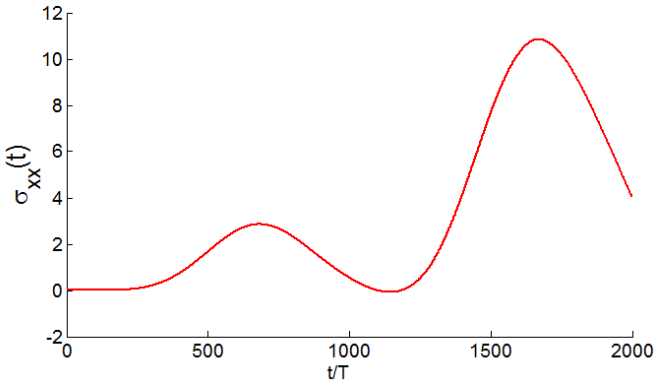

Fig. 4. Conductivity $\sigma_{xx}(t)$ in units of $e^2/\hbar$, see Eq. (19), as a function of time for a kicked graphene nanoribbon. Parameters are as in Fig. 3 but with kicking time period $T = 1$ fs.

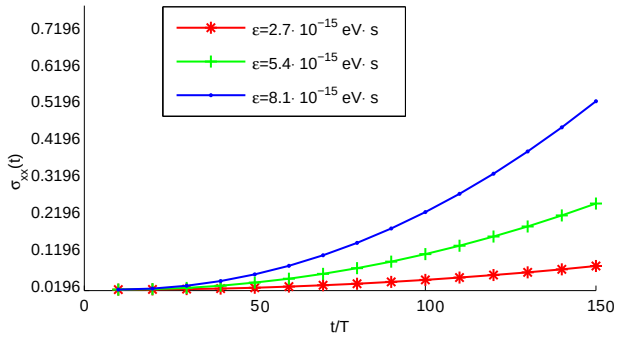

Fig. 5. Same as Fig. 4 but for several values of the kicking strength ε, and showing only the initial time period ($t < 150T$).

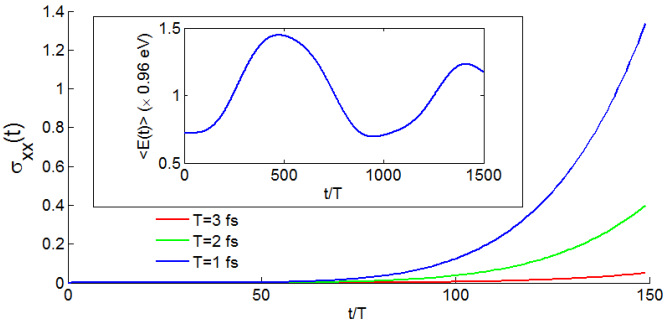

Fig. 6. Same as Fig. 5 but for different kicking periods T and the fixed kicking strength $\varepsilon = 2.7 \times 10^{-13}$ eVs. The inset shows the time dependence of the average kinetic energy on a longer time scale for $T = 1$ fs.

ε. However, as seen in Fig. 4, after a longer time span, the conductivity will be suppressed again. Nonetheless, the variation of the kicking strength allows for a considerable tunability of the conductivity.

The dependence of the conductivity on a variation of the kicking period T (with fixed strength ε) is illustrated by Fig. 6. We find that $\sigma_{xx}(t)$ monotonically grows within the considered time interval, although at larger

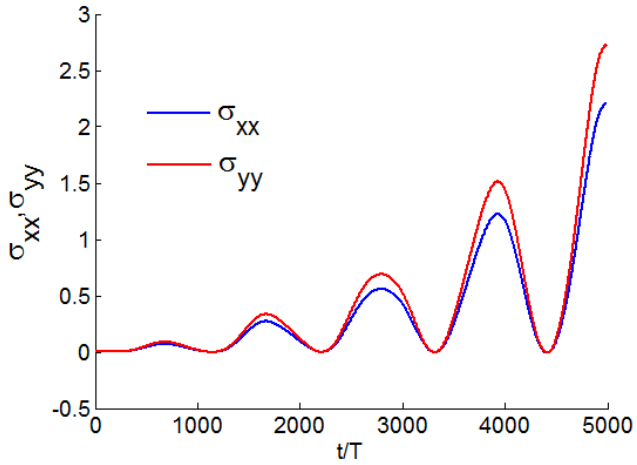

Fig. 7. Time-dependence of the longitudinal conductivities $\sigma_{xx}(t)$ and $\sigma_{yy}(t)$ (in units of $e^2/\hbar$) along the x- and y-direction, respectively, for the parameters in Fig. 4.

times (not shown) the conductivity decreases and becomes quasi-oscillatory again, as displayed before in Fig. 4. The inset of Fig. 6 also shows the time-dependence of the average kinetic energy,

$$\langle E(t)\rangle = \int_0^{L_x} dx \int_0^{L_y} dy\ \Psi^*(x,y,t) H_0 \Psi(x,y,t) = \sum_n |A_n(t)|^2 E_n. \quad (20)$$

This quantity exhibits time-periodic behavior, again reflecting the periodic appearance of band crossings as illustrated by Fig. 3. Such a behavior is different from a localization-induced saturation expected from quantum chaos theory but also differs from the simple monotonic growth expected on classical grounds [25,26,27].

Next, in Fig. 7, we compare the different components of the conductivity, namely $\sigma_{xx}(t)$ and $\sigma_{yy}(t)$. Although the kicking force acts along x-direction, we find very similar values for the conductivities in both directions. The spectral rearrangement caused by the kicking force is thus quite efficient in also inducing current fluctuations in the transverse (y) direction.

Finally, Fig. 8 presents the spatio-temporal evolution of the probability density, $|\Psi(x,y,t)|^2$. Since the result is homogeneous along the y-direction, we show it as 2D color-scale plot in the (x,t) plane; note the symmetry under spatial reflection with respect to the ribbon midpoint $x = L_x/2$. Figure 8 provides additional information about the possibility of spatio-temporal quantum localization of electrons in the kicked graphene nanoribbon. In fact, we conclude from Fig. 8 that the carriers are not fully localized inside the ribbon, although signatures of localization near the midpoint are visible for finite time spans.

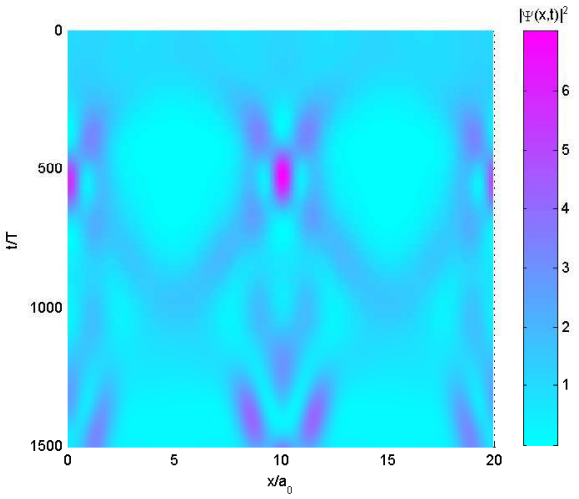

Fig. 8. Probability density as a function of time and coordinate for the parameters in Fig. 4 (note that $L_{=}20a_0$).

4 Concluding remarks

In this paper, we have studied time-dependent particle transport in graphene zigzag nanoribbons driven by an external time-periodic δ-kicking potential. The time-dependent Dirac equation can be solved exactly within a single kicking period, and numerical iteration of this solution provides access to the wave function at arbitrary time. Using this wave function, we have computed the time-dependent optical conductivity (and other quantities). The conductivity is observed to initially grow as a function of time up to certain time, after which the conductivity decreases and ultimately shows quasi-oscillatory behavior.

We find it rather remarkable that by judiciously choosing the strength ε and the time period T of the kicking field, one can achieve almost arbitrary results for the oscillation period and for the amplitude of the conductivity. In particular, it is possible to choose parameters such that the initial increase extends for very long time. The described behavior of $\sigma_{\alpha\alpha}(t)$ can be linked to the existence of (anti-)crossings in the quasienergy bands of the driven system.

The model studied in our work could be realized in zigzag ribbons made of monolayer graphene samples that are exposed to standing-wave ultrashort laser pulses, such as those discussed in Refs. [29,30,31]. The above results also may help in solving the problem of tunable charge transport in graphene-based electronic devices.

5 Acknowledgments

This work has been supported by the Volkswagen-Stiftung.

References

1. A.H. Casto Neto, F. Guinea, N.M.R. Perez, K.S. Novoselov, and A.K. Geim, Rev. Mod. Phys. **81**, 109 (2009).
2. N.M.R. Peres, Rev. Mod. Phys. **82**, 2673 (2010).
3. S. Das Sarma, S. Adam, E. H. Hwang, and E. Rossi, Rev. Mod. Phys. **83**, 407 (2011).
4. A.V. Rozhkov, G. Giavaras, Y.P. Bliokh, V. Freilikher, and F. Nori, Phys. Rep. **503**, 77 (2011).
5. A.H. Castro Neto and K. Novoselov, Rep. Prog. Phys. **74**, 082501 (2011).
6. V.N. Kotov, B. Uchoa, V.M. Pereira, F. Guinea, and A.H. Castro Neto, Rev. Mod. Phys. **84**, 1067 (2012).
7. J. Güttinger, F. Molitor, C. Stampfer, S. Schnez, A. Jacobsen, S. Dröscher, T. Ihn, and K. Ensslin, Rep. Prog. Phys. **75**, 126502 (2012).
8. A. Scholz, A. Lopez, and J. Schliemann, Phys. Rev. B **88**, 045118 (2013).
9. A. Vaezi, N. Abedpour, R. Asgari, A. Cortijo, and M.A.H. Vozmediano, Phys. Rev. B **88**, 125406 (2013).
10. A. Lopez, Z.Z. Sun, and J. Schliemann, Phys. Rev. B **85**, 205428 (2011).
11. K.-H. Ding, Z.-G. Zhu, and J. Berakdar, Phys. Rev. B **84**, 115433 (2011).
12. E. Perfetto, G. Stefanucci, and M. Cini, Phys. Rev. B **82**, 035446 (2010).
13. C.G. Rocha, L.E.F. Foa Torres, and G. Cuniberti, Phys. Rev. B **81**, 115435 (2010).
14. K.L. Ishikawa, Phys. Rev. B **82**, 201402, (2010).
15. S.E. Savelev, W. Häusler, and P. Hänggi, Phys. Rev. Lett. **109**, 226602 (2012).
16. T.M.Rusin and W. Zawadzki, Phys. Rev. B **80**, 045416 (2009).
17. C.H. Lui, K.F. Mak, J. Shan, and T.F. Heinz, Phys. Rev. Lett. **105**, 127404 (2010).
18. W.-T.Liu, S. W. Wu, P. J. Schuck, M. Salmeron, Y. R. Shen, and F. Wang, Phys. Rev. B **82**, 081408 (2010).
19. A. Roberts, D. Cormode, C. Reynolds, T. Newhouse-Illige, B.J. LeRoy, and A.S. Sandhu, Appl. Phys. Lett. **99**, 051912 (2011).
20. H.L. Calvo, H.M. Pastawski, S. Roche, and L.E.F. Foa Torres, Appl. Phys. Lett. **98**, 232103 (2011).
21. T. Li, L. Luo, M. Hupalo, J. Zhang, M.C. Tringides, J. Schmalian, and J. Wang, Phys. Rev. Lett. **108**, 167401 (2012).
22. H.K. Kelardeh, V. Apalkov, and M.I. Stockman, preprint arXiv:1401.5786.
23. H.K. Avetissian, A.K. Avetissian, G.F. Mkrtchian, and Kh.V. Sedrakian, Phys. Rev. B **85**, 115443 (2012).
24. P. Thalmeier, B. Dora, and K. Ziegler, Phys. Rev. B **81**, 041409(R) (2010).
25. G. Casati *et al.*, in *Lecture Notes in Physics* **93**, 334 (Springer, Berlin, 1979).
26. R. Sankaranarayanan and V.B. Sheorey, Phys. Lett. A **338**, 288 (2005).
27. G.M. Izrailev, Phys. Rep. **196**, 299 (1990).
28. L. Brey and H. A. Fertig, Phys. Rev. B **73**, 235411 (2006).
29. F.L. Moore, J.C. Robinson, C.F. Bharucha, B. Sundaram, and M.G. Raizen, Phys. Rev. Lett. **75**, 4598 (1995).
30. A. Ullah and M.D. Hoogerland, Phys. Rev. B **83**, 046218 (2012).
31. A. Ullah, S.K. Ruddell, J.A. Currivan, and M.D. Hoogerland, Eur. Phys. J. D **66**, 315 (2012).
32. A. Matos-Abiague and J. Berakdar, Phys. Rev. B **69**, 155304 (2004).
33. N. Tzoar and J.I. Gersten, Phys. Rev. B **12**, 1132 (1975).
34. A. Altland and B.D. Simons, *Condensed Matter Field Theory*, 2nd. edition (Cambridge University Press, Cambridge UK, 2010).